Article | Received 15 June 2026; Revised 18 June 2026; Accepted 18 June 2026; Published 30 June 2026
https://doi.org/10.55092/opr20260004

Arbitrary eigenmode reshaping induced by distributed non-reciprocity in non-Hermitian systems

Zhaomin Rong[1,†], Yu Chen[2,†], Yanan Bai[1], Tiejun Cui[2,*], Lei Zhou[3,4,5,*], Shuo Liu[2,*] and Shaojie Ma[1,3,5,*]

[1] College of Future Information Technology, Fudan University, Shanghai 200433, China
[2] State Key Laboratory of Millimeter Waves, Southeast University, Nanjing 210096, China
[3] Shanghai Key Laboratory of Metasurfaces for Light Manipulation, Shanghai 200433, China
[4] State Key Laboratory of Surface Physics and Department of Physics, Fudan University, Shanghai 200433, China
[5] Key Laboratory of Micro and Nano Photonic Structures (MOE), Fudan University, Shanghai 200433, China

† These authors contributed equally to this work.

* Correspondence authors; E-mails: tjcui@seu.edu.cn (T.C.); phzhou@fudan.edu.cn (L.Z.); liushuo.china@seu.edu.cn (S.L.); shaojiema@fudan.edu.cn (S.M.).

Highlights:

- A 1D framework maps arbitrary non-reciprocity distributions to mode reshaping.
- NHRE decouples global mode reshaping from spectral changes.
- Electrical circuits realize programmable asymmetric hopping profiles.
- Optical CROW simulations verify NHRE at optical frequencies.

Abstract: Periodic non-reciprocal systems have attracted significant attention for their striking non-Hermitian skin effect (NHSE) and the development of a comprehensive non-Bloch theory. In contrast, aperiodic non-reciprocal systems have been rarely explored, owing to the intrinsic complexity induced by spatial non-uniformity and absence of predictable physical behavior. Here, we establish a theoretical framework for one-dimensional nearest-neighbor lattices under open boundary conditions, and reveal that the spatially varying non-reciprocal coupling can be interpreted geometrically as a designable imaginary gauge field, providing a tunable metric on the Hilbert space that serves as a powerful and deterministic knob to control the wave-functions of eigenmodes. By tailoring the non-reciprocity distribution in this specific system, we combine theory, proof-of-concept electric-circuit experiments, and high-frequency optical-lattice simulations with micro-ring resonators to demonstrate that the eigenmodes of a non-Hermitian system can be reshaped into *arbitrary* spatial profiles without altering their spectral distribution, a mode-field engineering strategy termed non-Hermitian reshaping engineering (NHRE). In the special case of a uniform non-reciprocity distribution, NHRE

recovers the characteristic exponential mode localization in the conventional NHSE. While the full diagonalization framework underlying the inverse mapping is limited to one dimension, some of its design principles can be partially extended to arbitrary higher-dimensional systems, offering an efficient route to mode modulation and deepening our understanding of non-Hermitian physics.

Keywords: non-Hermitian reshaping engineering; distributed non-reciprocity; spectrum-preserving mode engineering; topological electrical circuits; coupled resonant optical waveguides

1. Introduction

Non-Hermitian theory establishes a powerful theoretical framework to model open systems, which can exchange energy with their surroundings [1–5]. This interaction allows for effects like gain, loss, and non-reciprocity, leading to a wide range of fascinating phenomena [6–9]. Among them, the non-Hermitian skin effect (NHSE) is one of the most representative consequences of non-reciprocal coupling [10–14]. In periodic lattices with intrinsic or effectively induced non-reciprocity, eigenstates that are extended under periodic boundary conditions become localized at open boundaries, forming skin modes [15–18]. This anomalous boundary sensitivity is understood through the topological origin of NHSE and non-Bloch bulk–boundary correspondence [19,20]. Related open-system dynamics of NHSE have also been theoretically analyzed [21]. NHSE has been experimentally validated across quantum, acoustic/phononic, electrical-circuit, and photonic platforms [22–26]. Building on this picture, non-Bloch band theory incorporating the generalized Brillouin zone (GBZ) is widely used to describe eigenstates under open boundary conditions (OBCs) in one-dimensional (1D) non-Hermitian systems with periodic non-reciprocal couplings [27–31]. In two and higher dimensions, NHSE behaviors vary significantly in different directions, leading to phenomena such as geometry-dependent skin effect [15,24,32]. In these cases, defining a GBZ becomes considerably more challenging, necessitating a more sophisticated amoeba formulation to study the non-Hermitian bands [33–35].

We note that the spatial distribution of non-reciprocity (*i.e.*, the site-dependent variation of the asymmetric hopping amplitudes), which is often overlooked in theories constrained by spatial periodicity, might constitute an important degree of freedom in non-Hermitian system. Even a simple step-like non-reciprocity distribution can reshape the eigenmode profiles, transforming non-Hermitian skin modes into spatially extended ones [36]. In some platforms, the non-reciprocity can even be externally controlled [37–41]. Such flexibility in non-reciprocity can lead to localization or delocalization of eigenstates. However, no theoretical framework is currently available to study such aperiodic systems and predict related fascinating phenomena. Current eigenmode analyses rely primarily on brute-force tight-binding model (TBM) calculations, which can face significant numerical issues when dealing with large non-Hermitian matrices.

Here, we rigorously demonstrate that, in a 1D nearest-neighbor non-reciprocal TBM model under OBCs, we can reshape the wavefunctions of all eigenmodes deterministically into *arbitrary* spatial profiles without altering their dispersion behavior by tailoring the non-reciprocity distribution. The algebraic foundation of this effect is the spectral invariance of finite tridiagonal matrices. Specifically, the eigenvalue spectrum of a 1D nearest-neighbor TBM Hamiltonian is uniquely determined by the product of its mutually reciprocal off-diagonal elements, *i.e.*, the geometric mean of the forward and backward hopping amplitudes, and is strictly invariant under any non-reciprocal redistribution that preserves this product. The spectrum-preserving reshaping of all eigenmodes directly follows from this invariance, with the diagonal similarity transformation serving as its explicit realization rather than its premise. Geometrically, this engineering framework arises from interpreting the spatially varying non-reciprocity as an imaginary vector potential, which corresponds to a tunable metric on the Hilbert space. This mechanism constitutes non-Hermitian reshaping engineering (NHRE). Rather than introducing an additional spectral effect, NHRE offers a distinct route for mode-field engineering: the target envelope is designed from the eigenvalue-invariance proof and then applied independently of the detailed profile of each mode. Furthermore, leveraging this geometric interpretation, NHRE provides a generalized framework to control mode distributions in arbitrary non-Hermitian systems, extending to two or three dimensions, beyond nearest neighbor coupling, and even in systems incorporating gain and loss. We experimentally demonstrate NHRE in 1D electric-circuit chains with engineered non-reciprocity distributions. By designing the coupling-capacitance matrix to implement site-dependent asymmetric hopping amplitudes, we show that different non-reciprocity distributions yield clear experimental signatures: the resonant frequencies remain nearly unchanged, whereas the measured impedance profiles are reshaped according to the designed envelope. The generality of the theory is further supported by simulations of optical lattices based on micro-ring resonators, confirming the universality of mode shaping through engineered non-reciprocal coupling.

2. Results

2.1. NHRE in a non-Hermitian SSH chain

We start with a concrete example: the reshaping engineering in a non-Hermitian Su-Schrieffer-Heeger (SSH) chain under open boundary conditions, which corresponds to the minimal setting implemented in our circuit experiment. This SSH chain is a specific realization of the general 1D nearest-neighbor non-reciprocal lattice sketched in Figure 1a, in which the hopping amplitudes, on-site potential, and complex gauge potential can be assigned site by site; here it is specialized to the SSH unit cell. The reciprocal SSH chain has alternating intracell and intercell hopping amplitudes v and w. Labeling the two sublattices in the nth unit cell as $|A_n\rangle$ and $|B_n\rangle$, the corresponding non-Hermitian Hamiltonian can be written as:

$$\begin{aligned} H = &\sum_{n=1}^{N} v\left(e^{-\kappa_{v,n}}|A_n\rangle\langle B_n| + e^{\kappa_{v,n}}|B_n\rangle\langle A_n|\right) \\ &+ \sum_{n=1}^{N-1} w\left(e^{\kappa_{w,n}}|A_{n+1}\rangle\langle B_n| + e^{-\kappa_{w,n}}|B_n\rangle\langle A_{n+1}|\right). \end{aligned} \tag{1}$$

Here, the factors $e^{-\kappa_{v,n}}$ and $e^{\kappa_{v,n}}$ (and likewise $e^{\pm\kappa_{w,n}}$ for the intercell bonds) encode the directional imbalance on each intracell bond: $\kappa_n = 0$ recovers reciprocal hopping, whereas $\kappa_n \neq 0$ produces unequal forward and backward hopping amplitudes. For simplicity, we employ a single ordered bond index κ_n to denote the non-reciprocity sequence across all SSH bonds, regardless of whether they are intracell or intercell. The spatial distribution of non-reciprocity is taken as $\kappa_n = -\alpha(n - r)$, where α controls the non-reciprocity gradient and r sets the spatial reference point.

This simple model already captures the central observation. As shown in Figure 1b,c, when α is varied at fixed SSH couplings, the entire energy spectrum remains completely unchanged, including the in-gap topological zero mode. Meanwhile, the gap closing and the associated topological transition at

$v = w$ persists, just as in the reciprocal SSH chain. The eigenmodes, however, undergo continuous reshaping. For the linear profile introduced above, all modes acquire a common Gaussian envelope of the form:

$$t_n = C \cdot \exp\left[-\frac{1}{2}\alpha \cdot (n - n_c)^2\right], \quad \text{with } n_c = r - 3/2 \tag{2}$$

Here, C is an overall normalization constant, and n_c is the envelope center determined by r. This expression directly governs the SSH response: α controls the localization strength, while r shifts the center position via n_c. As illustrated in Figure 1d,e, increasing α from 0 to 0.04 progressively concentrates both bulk and edge modes to the center. We note that although the same envelope acts on every eigenmode, bulk and edge states can display different apparent responses due to their distinct profiles in the parent SSH lattice.

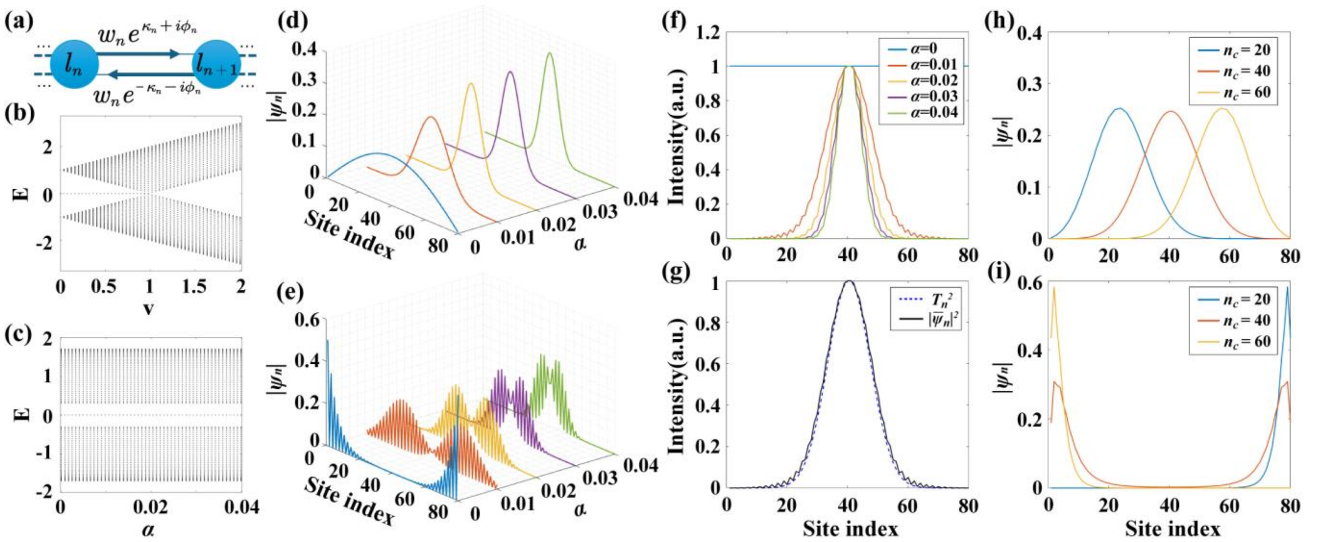

Figure 1. Schematic diagram of NHRE: **(a)** Lattice diagram of a general 1D non-Hermitian TBM model; **(b)** Energy spectrum of a finite SSH model with $\alpha = 0.02$ and $w = 1$, as a function of the intercell hopping amplitude v; **(c)** Energy spectrum of the same system for a fixed $v = 0.7$ and a varying α. Notably, arbitrary changes in $\kappa(n)$ do *not* affect the energy spectrum in this model, resulting in pure real energy spectrum despite the introduction of non-reciprocal hopping terms; **(d, e)** For $\kappa_n = -\alpha \cdot (n - r)$, the field distribution of **(d)** a typical bulk state and **(e)** degenerate edge states under varying α conditions, demonstrating that wavefunction $|\psi_n|$ gradually becomes more localized as α increases; **(f)** The incoherent mode distribution function $|\bar{\psi}_n|^2$, corresponding to the field distribution behavior in **(d, e)**, becomes increasingly localized as α increases; **(g)** Comparison of the envelope function and the incoherent mode distribution function for $\alpha = 0.04$ shows that the latter is significantly modulated by the former, resulting in a Gaussian mode centered in the middle of the system; **(h)** Representative field distribution for varying position parameter n_c. The center position of the wave function directly correlates with n_c; **(i)** Field distribution for negative α. Depending on n_c, the wave function localizes to the left, right, or both sides.

The corresponding incoherent mode distribution, shown in Figure 1f, is centered around n_c and becomes increasingly localized as α increases. The comparison in Figure 1g further shows that the analytically predicted envelope reproduces the numerical eigenstates with essentially no deviation. In fact, analysis reveals that this reshaping is programmable. Figure 1h shows that tuning r moves the intensity maximum to a target site; by tuning the sign and magnitude of α, one can steer the chain between extended, center-localized, and boundary-localized mode profiles. For negative α, all modes are instead pushed toward the two boundaries, as shown in Figure 1i. This concrete non-Hermitian SSH example motivates the more general, but constrained, one-dimensional formulation below.

2.2. Non-Hermitian reshaping engineering

2.2.1. Theoretical formulation in one dimension

Motivated by the non-Hermitian SSH chain, we next formulate a constrained 1D model, in which this reshaping mechanism is exact. We consider a generic 1D nearest-neighbor non-reciprocal TBM lattice under OBCs, wherein the hopping coefficient w_n, the on-site scalar potential l_n and the complex gauge potential $\phi_n + i\kappa_n$ can be varied freely, as shown in Figure 1a. The real part ϕ_n acts as a conventional vector potential introducing phase factors via Peierls substitution, while the imaginary part κ_n serves as a designable imaginary gauge potential that directly sets the non-reciprocal hopping amplitudes, taking the form $w_n e^{\kappa_n}$ and $w_n e^{-\kappa_n}$, respectively. κ_n is allowed to vary spatially with an arbitrary distribution, and we demonstrate that such a 1D nearest-neighbor non-reciprocal Hamiltonian under OBCs can always be mapped to a Hermitian counterpart.

The real space single-particle non-reciprocal Hamiltonian can be written as:

$$\begin{aligned}\mathbf{H} &= \sum_{m,n} H_{NR,mn} \cdot |m\rangle\langle n| \\ &= \sum_{n} w_n \left(e^{-\kappa_n - i\phi_n}|n\rangle\langle n+1| + e^{\kappa_n + i\phi_n}|n+1\rangle\langle n|\right) + l_n|n\rangle\langle n|\end{aligned} \tag{3}$$

Here, $|n\rangle$ denotes the orthonormal basis with a particle localized on site n. Under OBCs, the tridiagonal structure of H_{NR} guarantees that its eigenvalues are independent of the complex gauge potential $\phi_n + i\kappa_n$ (see Supplementary Materials for a mathematical proof). Since the spectrum is fixed, this invariance can be made explicit through a similarity transformation $\hat{T}$ applied to the basis of the system: $|n'\rangle \mapsto \hat{T}|n\rangle$. With this transformation, the Hamiltonian operator can be transformed to $\mathbf{H} = \sum_{m,n} H_{R,mn} \cdot |m'\rangle\langle n'|$, while $H_R = T^{-1} H_{NR} T$ and $H_{R,mn} = {t_m}^{-1} t_n H_{NR,mn}$. For the 1D nearest-neighbor non-reciprocal Hamiltonian H_{NR} in Equation (3) under OBCs, the required transformation matrix $\hat{T}$ is intrinsically diagonal, with its elements t_n satisfying the recurrence relationship $t_{n+1} = e^{\kappa_n} \cdot t_n$. Thus, H_{NR} and its reciprocal counterpart H_R share identical eigenvalue spectrum and Jordan normal structure, and their eigenstates are directly related through the similarity transformation. This mapping imparts a uniform, additional envelope function to all wavefunctions, comprehensively reshaping the spatial profiles of all eigenstates simultaneously, thereby establishing NHRE as a mode-decoupled engineering procedure.

For such a non-reciprocal model H_{NR}, the spectral features that diagnose topology, such as the presence, robustness, and energy of in-gap boundary/edge states, are preserved and can be fully determined by the corresponding reciprocal model H_R, even though eigenstate-based topological invariants for the original non-Hermitian system may change. Notably, while the spatial profile of the non-reciprocity breaks translational symmetry, rendering conventional bulk–boundary correspondence inapplicable to H_{NR} directly, the similarity transformation effectively gauges out this non-periodic modulation. This maps the open chain onto a virtual, translationally invariant Hermitian system. The energy spectrum and the protection of in-gap boundary states are thus rigorously guaranteed by the bulk–boundary correspondence of this underlying periodic Hermitian counterpart. Thus, NHRE operates as a spectrum-preserving mode engineering route rather than a tool for altering non-Hermitian topological classification.

Physically, this NHRE framework admits a natural geometric interpretation when viewed through the lens of gauge field theory. The asymmetric hopping magnitude κ_n acts as an imaginary vector potential, controlling the exponential envelope of wavefunctions through the similarity transformation matrix T. From this perspective, a spatially distributed complex gauge field $\phi_n + i\kappa_n$ emerges naturally, with ϕ_n governing the phase accumulation and κ_n dynamically sculpting the mode amplitudes. This geometric language offers a unified baseline for NHRE, connecting the spatially distributed non-reciprocity to the imaginary gauge field description of non-reciprocal lattices and to the biorthogonal formulation of non-Hermitian systems, and making explicit that the eigenmode envelopes are reshaped while the spectrum is preserved.

Crucially, NHRE shifts the paradigm from the rigid boundary accumulation characteristic of the standard NHSE, to a highly reconfigurable engineering degree of freedom enabled by spatially non-uniform non-reciprocity. This framework successfully unifies several known non-Hermitian phenomena as operating regimes. When $\kappa_n = \kappa_0$ is a constant, the envelope function of NHRE simplifies to a pure exponential, naturally recovering the characteristic boundary localization that hallmarks conventional NHSE under OBCs [20]. Alternatively, when $\kappa_n = -\kappa_0 \cdot \Theta(n_0 - n)$ is configured as a step function, NHRE reproduces non-Hermitian morphing [36], where the tailored envelope exactly counteracts the intrinsic decay of topological edge states, delocalizing them into extended modes that occupy the entire bulk lattice. Going beyond these piecewise configurations, the true versatility of this geometric perspective becomes apparent when allowing κ_n to vary continuously, yielding arbitrary mode reshaping as exemplified by the linear case above.

2.2.2. Generalization to higher dimensions

We note that the localization induced by a linear κ_n modulation is merely a special case of NHRE. In general, the mode-field envelope function can take arbitrary forms, even complex ones with additional phase. Geometrically, this flexibility reflects the role of $\phi_n + i\kappa_n$ as a complex gauge potential that shapes the Hilbert-space metric independently. For systems with other forms of non-Hermiticity, such as gain and loss, the similarity transformation preserves the full eigenvalue spectrum and Jordan normal structure of the Hamiltonian, effectively reducing the system to an equivalent model containing only on-site gain and loss.

Moreover, in more general TBM settings, such as higher dimensions, long-range couplings, or periodic systems, the tridiagonal matrix structure that guarantees the invertible mapping is broken and a well-defined metric extracted from an arbitrary H_{NR} may not exist. However, we stress that this restriction applies only to the inverse problem of extracting a Hermitian parent from an arbitrarily prescribed non-reciprocal Hamiltonian, which indeed becomes over-constrained once next-nearest-neighbor or longer-range couplings are present. It does not limit the forward construction that underlies all of our higher-dimensional and beyond-nearest-neighbor results. The forward mode-field engineering approach, constructing H_{NR} from a known reference Hamiltonian H_R and a desired envelope T, remains fully operational. Starting from any reference Hamiltonian H_R with known spectral features, mode distribution, and topologically protected boundary states (if any), one can implement a desired complex field envelope $t_n \in \mathbb{C}$ to define the metric of the Hilbert space, and thereby reshape the mode profiles by constructing a transformed Hamiltonian $H_{NR} = TH_RT^{-1}$. Compared with the original reference model H_R, the modified model H_{NR} includes additional non-reciprocal and phase terms in the off-diagonal elements. Despite these modifications, owing to the inherent invariance of the similarity transformations, the energy spectrum and the spectral fingerprints of topology (e.g., the presence of in-gap boundary states) remain unchanged. This indicates that, while the modified Hamiltonian model H_{NR} preserves topologically protected zero modes within a band gap, the spatial profiles of the edge/boundary modes can be flexibly reshaped through the engineered non-reciprocity distributions without re-solving the individual eigenmodes. Such tunability is highly promising, particularly for applications in topological lasers, sensors, and wave manipulation devices [38,42,43].

As an example, we illustrate the modulation of eigenfunctions in a two-dimensional BBH model [44,45], which behaves as a higher-order topological insulator (HOTI), as shown in Figure 2a. A slight onsite modulation is introduced at the four corners, lifting the corner-mode degeneracy while preserving their topological nature within the bandgap. For an initial corner state $\psi_0(m,n)$ shown in Figure 2c, the envelope function can be tailored to be $t_{m,n} = \psi_{NHRE}(m,n) \cdot {\psi_0}^{-1}(m,n)$ for any desired mode distribution $\psi_{NHRE}(m,n)$. These $t_{m,n}$ values induce a series of distinct non-Hermitian configurations, each retaining nearest-neighbor coupling yet exhibiting a unique eigenfunction. For the special field distribution shown in Figure 2d–g, the energy spectra of the corresponding non-reciprocal Hamiltonians H_{NR} remain unchanged, as depicted in Figure 2b. Notably, the phase distribution of the eigenmodes can also be independently modulated in the same process. The phase pattern illustrated in Figure 2h corresponds to the eigenfunction reshaped into the form of the three letters “FDU” in Figure 2g, varying continuously from $-\pi$ to π around the center.

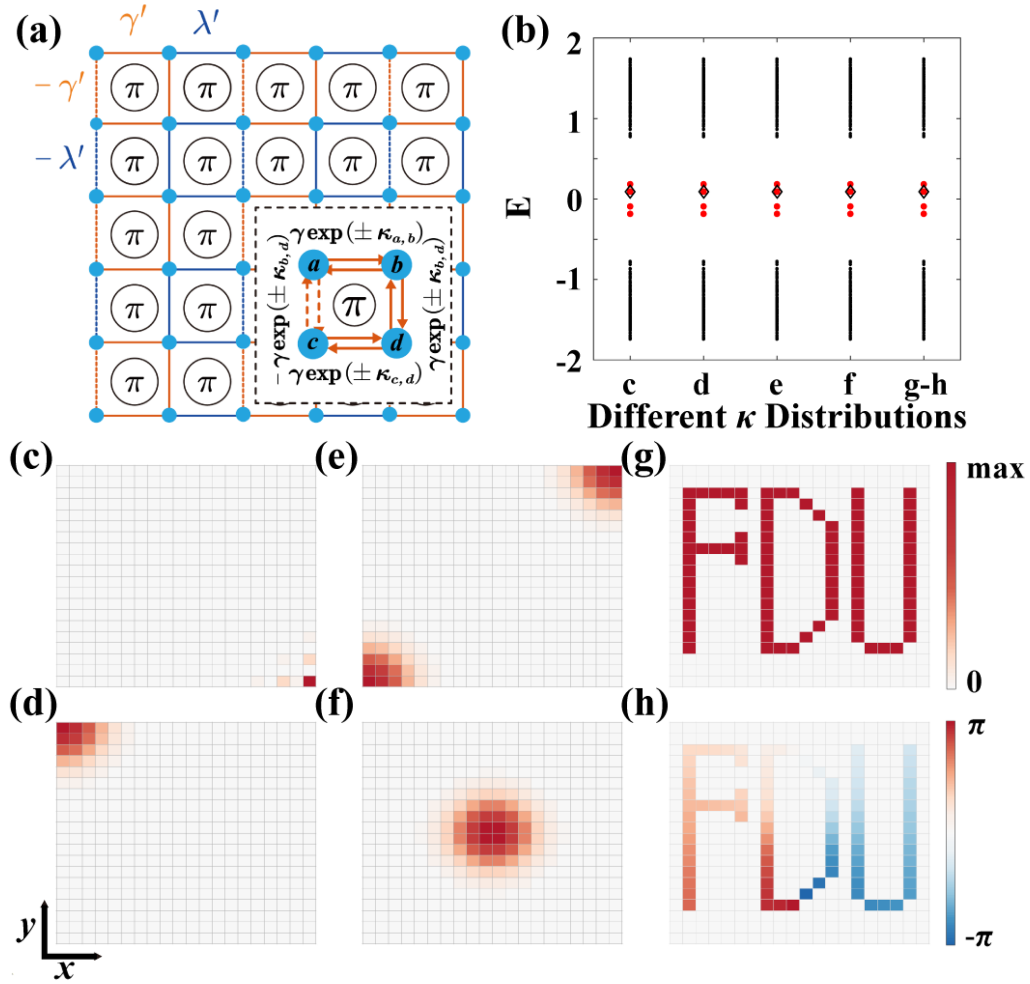

Figure 2. Modulation of HOTI states via non-reciprocal control: **(a)** The BBH model with non-reciprocal couplings introduced, where each hopping coefficient appears in pairs of the form $\exp(\pm\kappa_{n,m})$; **(b)** Energy band diagram of five modified BBH models with different κ distributions. The diamond markers indicate the modulated corner states. The abscissa represents five different κ distributions, corresponding to panels **(c–h)**. The eigen-energies remain unchanged across different κ distributions; **(c)** Field distribution of a corner state in the original BBH model configuration; **(d–h)** Reshaping of the corner state towards: **(d)** another corner, **(e)** two corners, **(f)** the interior and **(g–h)** special patterns with modified amplitude and phase distribution; **(h)** Phase diagram corresponding to **(g)**, showing a continuous variation from $-\pi$ to π of the phase distribution of the "FDU"-shaped eigenfunction.

2.3. Experimental demonstration in topological circuits

Electrical circuits offering high design flexibility provide a powerful and versatile platform for exploring non-Hermitian physics [46–50]. Recent circuit studies have further revealed rich topological and nonlinear dynamics [51]. Figure 3a,b illustrates a topological circuit architecture that realizes non-Hermitian SSH models with programmable non-reciprocal couplings. Each node is grounded through a parallel inductor-capacitor (LC) resonator, with adjacent nodes coupled via non-reciprocal capacitors implemented using active voltage followers. By designing the feedback and coupling capacitor ratios, the circuit can reliably realize non-reciprocity parameters in the range $-4 \le \kappa(n) \le 4$, sufficient to implement all modulation profiles demonstrated in this work. By toggling the dual in-line package (DIP) switches to select different capacitor configurations, the 20-unit-cell circuit can be reconfigured into multiple states, each associated with a distinct non-Hermitian Hamiltonian H_{NR}.

The response of the electrical circuit is analyzed using nodal analysis, which relates the total input current I_a at node a to the voltages V_b at all other nodes:

$$I_a = \sum_b J_{ab}(w) \cdot V_b \tag{4}$$

The admittance matrix J, also denoted as circuit Laplacian in physics, encodes the entire configuration of the circuit, including connectivity and component values:

$$J(\omega) = i\omega C \cdot H_{NR} + \left(i\omega C_t + \frac{1}{i\omega L_t}\right) \cdot I = i\omega C \cdot [H_{NR} - \lambda(\omega) \cdot I] \tag{5}$$

Here, C_t and L_t represent the Laplacians of the onsite LC-resonators at each node, while C denotes the unit coupling capacitance. The quantity $\lambda(\omega) = -1/C \cdot (C_t - 1/\omega^2 L_t)$ defines the resonance frequency scale, thereby linking the circuit frequency ω to the Hamiltonian eigenfrequency E. The effective matrix H_{NR}, engineered through the non-reciprocal capacitor distributions, is exactly the same as the designed non-reciprocal SSH models.

The mutual impedance Z_{ab} between nodes a and b is expressed as:

$$Z_{ab}(w) = [J^{-1}(w)]_{ab} = \frac{1}{i\omega C} \cdot \sum_n \frac{\Psi_{bn}^* t_b^{-1}}{E_n - \lambda(\omega)} \cdot t_a \Psi_{an} \tag{6}$$

Here, Ψ_n is the eigenstate of the corresponding Hermitian Hamiltonian H_R. Near resonance, when $E_n \approx \lambda(\omega)$, the summation is dominated by the $n-th$ term, and $Z_{ab}(\omega_n)$ captures the spatial profile of $n-th$ eigenmode of the non-reciprocal Hamiltonian H_{NR}, *i.e.*, $Z_{ab}(\omega_n) \propto t_a \Psi_{an}$. Consequently, the eigenfrequencies and eigenmodes appear as resonant peaks and spatial distributions in the mutual impedance spectrum, which can be directly measured through standard transmission measurements using a vector network analyzer. The choice of node b only modifies the mode-dependent normalization factor, without affecting the resonance frequency or the relative amplitude distribution. To mitigate intensity variations across modes, we redefine the summed mutual impedance $\tilde{Z}_a$ by summing Z_{ab} over all nodes b, *i.e.*, $\tilde{Z}_a = \sum_b |Z_{ab}|$, thereby characterizing the circuit's spatial and frequency response.

For a Hermitian SSH model ($\alpha = 0$), the simulated $\tilde{Z}_a$ distribution exhibits discrete resonant peaks, with spatial profiles reproducing the characteristic mode localization of the Hermitian SSH model, as shown in Figure 3c. However, in the raw experimental spectrum shown in Figure 3d, these peaks are broadened and partially overlapping due to parasitic resistance. To account for this effect, we applied a deterministic compensation scheme that, analogous to the complex-frequency approach [52–55], removes the influence of parasitic resistance. The method calibrates the measured self-admittance against the lossless reference condition (*i.e.*, purely imaginary self-admittance). This procedure is uniquely determined by the experimental data and requires no adjustable parameters, allowing clear identification of individual modes, as shown in Figure 3e,f.

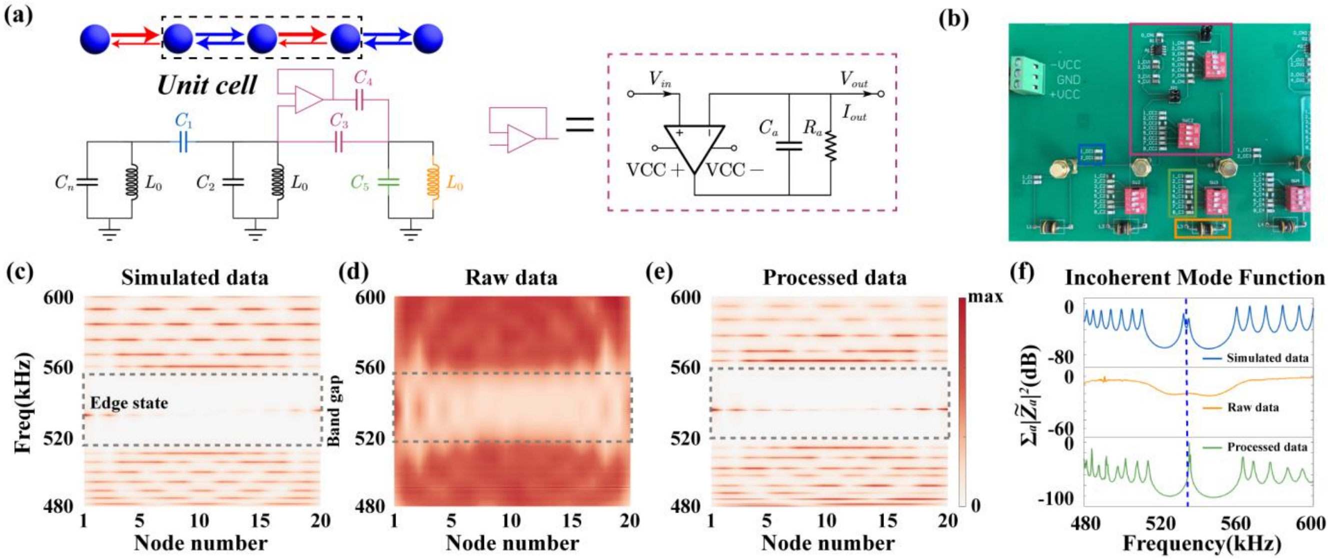

Figure 3. Experimental implementation of NHRE in a non-Hermitian electrical circuit: **(a)** Schematic of the non-Hermitian circuit with fixed inductance ($47\ \mu H$) and position-dependent capacitance. Non-reciprocal coupling is implemented via operational amplifiers (purple dashed box) configured as voltage followers; **(b)** Photograph of the fabricated circuit board. Color-coded frames correspond to components in **(a)**: non-reciprocal capacitive hopping (pink), reciprocal capacitive coupling (blue), and capacitor–inductor oscillator nodes (green/orange); **(c)** Numerically simulated spectrum of the summed mutual impedance $\tilde{Z}_a$, with frequency on the vertical axis and the lattice position on the horizontal axis; **(d)** Measured $\tilde{Z}_a$ spectrum, exhibiting loss-induced broadening and mode overlap, primarily from inductor parasitic resistance; **(e)** Processed experimental data after de-embedding parasitic effect, resolving individual eigenmodes with significantly reduced linewidths; **(f)** Incoherent mode distribution function *versus* frequency, with peaks corresponding to resonant frequency satisfying $E_n = \lambda(\omega_n)$.

Figure 4a–d displays the $\tilde{Z}_a$ spectra for four representative circuits with $\alpha = 0, 0.02, 0.04$ and -0.04, respectively. Theoretically, the resonance frequency is independent of α, whereas the mode distribution, as reflected by the spatial profile of $\tilde{Z}_a$, localizes progressively toward the center for positive α and toward both edges for negative α. Clearly, as α increases from 0 to 0.04, the eigenstates become increasingly concentrated at the center due to the localization of the non-Hermitian envelope function. In contrast, for $\alpha = -0.04$, the envelope diverges in a squared-exponential manner toward both ends, pushing the eigenstates to the circuit edges. All modes, whether bulk or edge states, evolve in the same manner, consistent with the theoretical results in Figure 1d,e. Figure 4e shows the distribution of the corresponding incoherent mode function $\sum_a |\tilde{Z}_a|^2$. The peak positions, which correspond to the resonant frequencies of the eigenmodes, remain unchanged for different values of α within experimental error, indicating that the non-reciprocal modulation preserves the system's eigenvalues regardless of the distribution profile. For a more detailed comparison, Figure 4f–h presents the distributions of representative bulk and edge states, where the dotted curves denote theoretical predictions, and the scattered solid lines represent experimental measurements. Although bulk states exhibit slight deviations from simulations due to intrinsic loss-induced overlap and residual imperfections, the reshaping behavior under non-reciprocal modulation remains faithfully captured. Edge states, being well isolated within the bandgap, show excellent agreement with theoretical predictions. The strong consistency observed in both bulk and edge states, along with the invariance of eigenfrequencies, provides solid verification of NHRE.

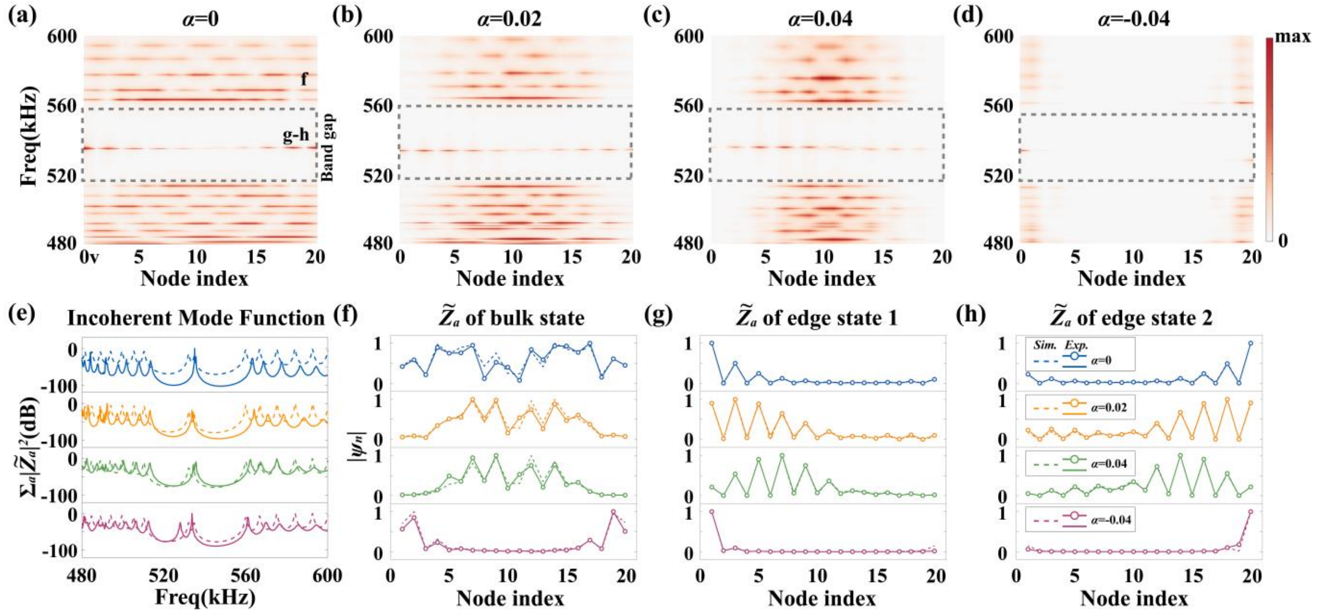

Figure 4. Measured impedance spectra illustrating NHRE under varying non-reciprocity distributions: **(a–c)** Measured summed mutual impedance $\tilde{Z}_a$ spectra for **(a)** $\alpha = 0$, **(b)** $\alpha = 0.02$, **(c)** $\alpha = 0.04$, showing progressively enhanced center-localized eigenstates with increasing α; **(d)** $\tilde{Z}_a$ spectrum for $\alpha = -0.04$, revealing double edge-localized eigenstates and direction-reversed NHRE; **(e)** Incoherent mode distribution function versus frequency, demonstrating invariant resonant frequencies under varying non-reciprocal modulations; **(f–h)** Evolution of representative bulk and edge states for different α, with simulations shown as dotted curves and experimental data as scattered solid lines. The simulation setup is slightly adjusted to lift the edge-state degeneracy and match experimental conditions.

2.4. Photonic implementation in optical waveguides

The NHRE concept can be further extended to optical frequencies using coupled resonant optical waveguides (CROWs), as shown in Figure 5a [56,57]. CROWs are composed of site rings with radius R_1 and link rings with radius R_2, where the clockwise (CW) modes in adjacent site rings are coupled via counterclockwise (CCW) modes in the link ring, and vice versa. The radii R_1 and R_2 are deliberately chosen to be different to prevent unwanted interference, while the gaps g_i are tuned to implement distinct SSH coupling strengths v and w. The coupling pathway depends on the propagation direction. To achieve non-reciprocal coupling, optical gain $(+i\gamma)$ is introduced in the upper half of the link ring, while an equivalent loss $(-i\gamma)$ is introduced in the lower half. This asymmetric gain-loss distribution generates directional-dependent asymmetric interactions, thereby realizing non-reciprocal coupling in the CROW model. Notably, the non-reciprocity parameter κ acquires opposite signs for the CW and CCW modes in the site rings. By increasing γ, the coupling strengths v and w remain nearly unchanged, while the non-reciprocity κ increases monotonically, as shown in Figure 5b.

This tunability allows for the realization of a linear non-reciprocity profile $\kappa_n = \pm\,\alpha \cdot (n - r)$ $(\alpha > 0)$, where '+' and '−' signs correspond to the CCW and CW modes, respectively. The simulated mode profiles are shown in Figure 5c–e, compared with the Hermitian case at $\gamma = 0$. While the eigenvalues remain nearly unchanged, NHRE induces pronounced reshaping of both bulk and edge modes. In particular, the CCW modes accumulate at the boundaries, whereas the CW modes localize toward the center, forming a Gaussian-like wave packet. These mode profiles confirm the effectiveness of NHRE as mode-field engineering at optical frequencies and suggest a promising route toward shaping laser resonators.

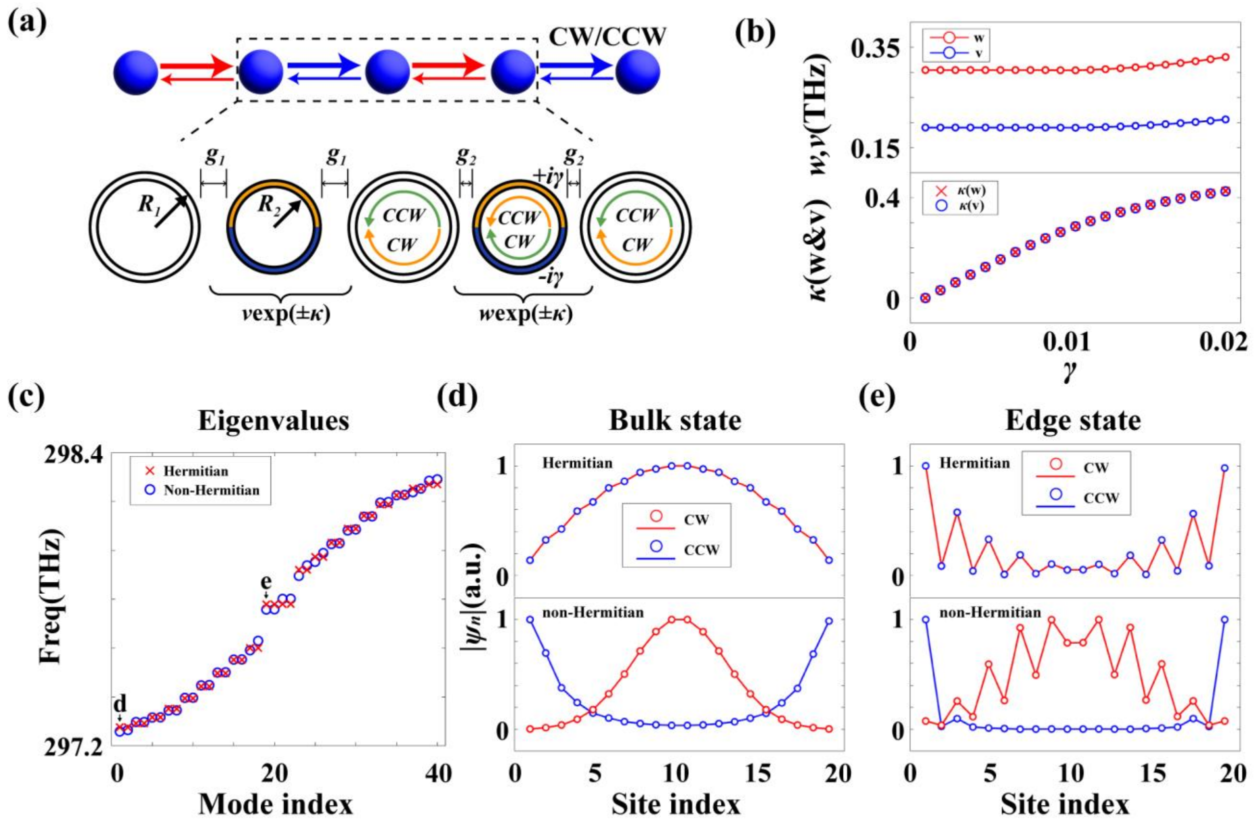

Figure 5. Simulated optical demonstration of NHRE in 1D non-Hermitian CROWs: **(a)** Schematic of the CROWs, consisting of site rings (radius $R^1 = 1.653\ \mu m$) and link rings (radius $R^2 = 1.565\ \mu m$) with a width of $0.2\ \mu m$. Coupling strengths v and w are tuned via inter-ring distance ($g_1 = 0.06\ \mu m$ and $g_2 = 0.04\ \mu m$), while non-reciprocity is introduced through optical gain $(+i\gamma)$ and loss $(-i\gamma)$; **(b)** Variation of the SSH coupling strengths v and w and the non-reciprocity κ as a function of γ; **(c)** Comparison of eigenvalue spectra between the non-Hermitian and Hermitian models; **(d, e)** Mode distributions for representative **(d)** bulk and **(e)** edge states, illustrating the NHRE-engineered localization: CW modes toward the center and CCW modes at the boundaries.

3. Discussion

In summary, we establish NHRE as a mode-field reshaping engineering framework by investigating the impact of an arbitrary non-reciprocity distribution in a 1D non-Hermitian TBM model under OBCs. This engineering strategy, extendable to arbitrary dimensions, enables precise control of mode-field profiles in aperiodic systems by shaping the Hilbert-space metric, allowing their eigenstates to be reshaped into arbitrary field distributions without altering their eigenvalues or the spectral fingerprints of topology. We experimentally demonstrate NHRE in electric-circuit systems and numerically verify it in optical CROWs. By exploiting topological edge or corner modes, NHRE enables flexible field engineering at topologically isolated eigenfrequencies.

Looking forward, NHRE provides, on the basis of the eigenvalue-invariance proof, a general framework for decoupling mode-field engineering from spectral and topological constraints in non-Hermitian systems. This capability may enable new strategies for robust wave manipulation in the presence of disorder and imperfections, as well as programmable control of mode localization in higher-dimensional lattices. Furthermore, extending NHRE to nonlinear or time-modulated platforms may allow dynamic control of mode localization and interactions, opening new avenues for exploring nonequilibrium phenomena in non-Hermitian topology.

4. Materials and methods

4.1. Numerical compensation of parasitic resistance

Parasitic resistance R_t, primarily from inductors, reduces quality factors, resulting in substantial spectrum broadening and overlapping between adjacent modes. To account for this effect, we apply an approach analogous to the complex-frequency method [52–55] to compensate for the influence of parasitic resistance on the measured spectra. The procedure is fully deterministic, uniquely determined by the experimental data, and involves no adjustable parameters.

In the experiment, the compensated impedance spectrum $Z(\omega)$ can be obtained through the following procedure:

$$Z(\omega)=\left\{{z_0}^{-1}\cdot[I-S(\omega)]\cdot[I+S(\omega)]^{-1}+\mathrm{diag}[J_C(n,\omega)]\right\}^{-1} \tag{7}$$

Here, $S(\omega)$ denotes the measured transmission spectrum matrix of the entire circuit, and $J_C(n,\omega)$ is a spatially and frequency-dependent equivalent gain used to compensate for the effect of parasitic resistance. Its values are extracted from the self-admittance $J_{nn}(\omega)$, measured via transmission spectra, by imposing the fundamental condition for a passive lossless circuit: the self-impedance must be purely imaginary. This constraint leads to a direct algebraic determination of $J_C(n,\omega)$, involving no fitting, optimization, or manual choice.

After compensation by $J_C(n,\omega)$, the loss components in the diagonal entries are eliminated, resulting in a mutual-impedance spectrum that closely matches the lossless ideal model, as shown in Figure 3e. We also verify the robustness and determinism of this procedure numerically, as shown in the Supplementary Materials. Even in regimes of strong modal overlap, the correction restores well-resolved spectral features. Further evidence is provided by the incoherent mode distribution shown in Figure 3f, where each peak corresponds to a measured resonant frequency satisfying $E_n=\lambda(\omega_n)$. The raw experimental data (orange curve) show mode overlap caused by losses, whereas the processed data (green curve) closely follows the theoretical predictions (blue curve) for most modes. These agreements, within experimental uncertainty, confirm the validity and robustness of the numerical compensation method.

Supplementary data

Supplementary materials include detailed theoretical derivations of non-Hermitian reshaping engineering, numerical verifications in 1D non-Hermitian SSH and 2D BBH models, additional analyses of topological circuit implementation and impedance-based mode measurements, the experimental loss-compensation/data-processing procedure, and full-wave simulations of non-Hermitian modulated coupled resonant optical waveguides. Supplementary Figures S1–S9 provide supporting numerical, experimental, and simulation results.

Data availability statement

The data and custom codes that support the findings of this study are openly available from Science Data Bank at https://doi.org/10.57760/sciencedb.32961.

Declaration of generative AI and AI-assisted technologies

During the preparation of this manuscript, the authors used ChatGPT only to improve language and readability. After using this tool, the authors reviewed and edited the content as needed and take full responsibility for the content of the manuscript.

Acknowledgments

Funding: This work was supported by National Key Research and Development Program of China (Grants No. 2023YFA1407700, 2023YFA1406901, 2022YFA1404903, 2022YFA1404700), National Natural Science Foundation China (Grants No. 12374343, 62288101, 62201136, 12221004), Natural Science Foundation of Shanghai (23dz2260100), the Start-up Research Fund of Fudan University (JIH1232133Y), and the Start-up Research Fund of Southeast University (Grant No. RF1028623117).

Authors' contribution

Conceptualization, S.M.; methodology, Z.R., Y.B., S.L. and S.M.; software, Z.R.; validation, Z.R., Y.C., S.L. and S.M.; formal analysis, Z.R., Y.B. and S.M.; investigation, Z.R., Y.B., Y.C., S.L. and S.M.; resources, S.L., S.M., L.Z. and T.J.C.; data curation, Z.R., Y.B., Y.C. and S.L.; writing—original draft preparation, Z.R., Y.C., S.L. and S.M.; writing—review and editing, all authors; visualization, Z.R. and Y.C.; supervision, S.M., S.L., L.Z. and T.J.C.; project administration, S.M., S.L., L.Z. and T.J.C.; funding acquisition, S.M., S.L., L.Z. and T.J.C. All authors have read and agreed to the published version of the manuscript.

Conflicts of interest

Lei Zhou holds the position of Editor-in-Chief for *Optics and Photonics Research* and has not peer reviewed or made any editorial decisions for this paper.

References

[1] Lin Q, Yi W, Xue P. Manipulating directional flow in a two-dimensional photonic quantum walk under a synthetic magnetic field. *Nat. Commun.* 2023, 14(1):6283.

[2] Makris KG, El-Ganainy R, Christodoulides DN, Musslimani ZH. Beam dynamics in PT symmetric optical lattices. *Phys. Rev. Lett.* 2008, 100(10):103904.

[3] Regensburger A, Bersch C, Miri MA, Onishchukov G, Christodoulides DN, *et al*. Parity-time synthetic photonic lattices. *Nature* 2012, 488(7410):167–171.

[4] Tuniz A, Wieduwilt T, Schmidt MA. Tuning the effective PT phase of plasmonic eigenmodes. *Phys. Rev. Lett.* 2019, 123(21):213903.

[5] Zhao H, Qiao X, Wu T, Midya B, Longhi S, *et al*. Non-Hermitian topological light steering. *Science* 2019, 365(6456):1163–1166.

[6] Bender CM, Brody DC, Jones HF. Complex extension of quantum mechanics. *Phys. Rev. Lett.* 2002, 89(27):270401.

[7] Wang H, Xiao Y, Zhang Z, Chan C, Lei D. Interconversion of exceptional points between different orders in non-Hermitian systems. *New J. Phys.* 2022, 24(11):113042.

[8] Ding K, Ma G, Xiao M, Zhang Z, Chan C. Emergence, coalescence, and topological properties of multiple exceptional points and their experimental realization. *Phys. Rev. X* 2016, 6(2):021007.

[9] Kawabata K, Shiozaki K, Ueda M, Sato M. Symmetry and topology in non-Hermitian physics. *Phys. Rev. X* 2019, 9(4):041015.

[10] Guo S, Dong C, Zhang F, Hu J, Yang Z. Theoretical prediction of a non-Hermitian skin effect in ultracold-atom systems. *Phys. Rev. A* 2022, 106(6):L061302.

[11] Li C, Trauzettel B, Neupert T, Zhang S. Enhancement of second-order non-Hermitian skin effect by magnetic fields. *Phys. Rev. Lett.* 2023, 131(11):116601.

[12] Li Z, Wang L, Wang X, Lin Z, Ma G, *et al*. Observation of dynamic non-Hermitian skin effects. *Nat. Commun.* 2024, 15(1):6544.

[13] Lin R, Tai T, Li L, Lee CH. Topological non-Hermitian skin effect. *Front. Phys.* 2023, 18(5):53605.

[14] Teo HT, Mandal S, Long Y, Xue H, Zhang B. Pseudomagnetic suppression of non-Hermitian skin effect. *Sci. Bull* 2024, 69(11):1667–1673.

[15] Zhang K, Yang Z, Fang C. Universal non-Hermitian skin effect in two and higher dimensions. *Nat. Commun.* 2022, 13(1):2496.

[16] Huang X, Lu C, Liang C, Tao H, Liu Y. Loss-induced nonreciprocity. *Light Sci. Appl.* 2021, 10(1):30.

[17] Yao S, Song F, Wang Z. Non-Hermitian Chern bands. *Phys. Rev. Lett.* 2018, 121(13):136802.

[18] Liu G, Mandal S, Zhou P, Xi X, Banerjee R, *et al*. Localization of chiral edge states by the non-Hermitian skin effect. *Phys. Rev. Lett.* 2024, 132(11):113802.

[19] Okuma N, Kawabata K, Shiozaki K, Sato M. Topological origin of non-Hermitian skin effects. *Phys. Rev. Lett.* 2020, 124(8):086801.

[20] Yao S, Wang Z. Edge states and topological invariants of non-Hermitian systems. *Phys. Rev. Lett.* 2018, 121(8):086803.

[21] Song F, Yao S, Wang Z. Non-Hermitian skin effect and chiral damping in open quantum systems. *Phys. Rev. Lett.* 2019, 123(17):170401.

[22] Xiao L, Deng T, Wang K, Zhu G, Wang Z, *et al*. Non-Hermitian bulk–boundary correspondence in quantum dynamics. *Nat. Phys.* 2020, 16(7):761–766.

[23] Zhang L, Yang Y, Ge Y, Guan Y, Chen Q, *et al*. Acoustic non-Hermitian skin effect from twisted winding topology. *Nat. Commun.* 2021, 12(1):6297.

[24] Zhou Q, Wu J, Pu Z, Lu J, Huang X, *et al*. Observation of geometry-dependent skin effect in non-Hermitian phononic crystals with exceptional points. *Nat. Commun.* 2023, 14(1):4569.
[25] Zou D, Chen T, He W, Bao J, Lee CH, *et al*. Observation of hybrid higher-order skin-topological effect in non-Hermitian topolectrical circuits. *Nat. Commun.* 2021, 12(1):7201.
[26] Lin Z, Song W, Wang L, Xin H, Sun J, *et al*. Observation of topological transition in Floquet non-Hermitian skin effects in silicon photonics. *Phys. Rev. Lett.* 2024, 133(7):073803.
[27] Deng T, Yi W. Non-Bloch topological invariants in a non-Hermitian domain wall system. *Phys. Rev. B* 2019, 100(3):035102.
[28] Guo C, Liu C, Zhao X, Liu Y, Chen S. Exact solution of non-Hermitian systems with generalized boundary conditions: size-dependent boundary effect and fragility of the skin effect. *Phys. Rev. Lett.* 2021, 127(11):116801.
[29] Guo G, Bao X, Tan L. Non-Hermitian bulk-boundary correspondence and singular behaviors of generalized Brillouin zone. *New J. Phys.* 2021, 23(12):123007.
[30] Ji X, Yang X. Generalized bulk-boundary correspondence in periodically driven non-Hermitian systems. *J. Phys. Condens. Matter* 2024, 36(24):243001.
[31] Yang Z, Zhang K, Fang C, Hu J. Non-Hermitian bulk-boundary correspondence and auxiliary generalized Brillouin zone theory. *Phys. Rev. Lett.* 2020, 125(22):226402.
[32] Wang W, Hu M, Wang X, Ma G, Ding K. Experimental realization of geometry-dependent skin effect in a reciprocal two-dimensional lattice. *Phys. Rev. Lett.* 2023, 131(20):207201.
[33] Hu H. Topological origin of non-Hermitian skin effect in higher dimensions and uniform spectra. *Sci. Bull* 2025, 70(1):51–57.
[34] Zhang K, Shu C, Sun K. Algebraic non-Hermitian skin effect and generalized Fermi surface formula in arbitrary dimensions. *Phys. Rev. X* 2025, 15(3):031039.
[35] Wang H, Song F, Wang Z. Amoeba formulation of non-Bloch band theory in arbitrary dimensions. *Phys. Rev. X* 2024, 14(2):021011.
[36] Wang W, Wang X, Ma G. Non-Hermitian morphing of topological modes. *Nature* 2022, 608(7921):50–55.
[37] Zhang Z, Qiao X, Midya B, Liu K, Sun J, *et al*. Tunable topological charge vortex microlaser. *Science* 2020, 368(6492):760–763.
[38] Gao Z, Qiao X, Pan M, Wu S, Yim J, *et al*. Two-dimensional reconfigurable non-Hermitian gauged laser array. *Phys. Rev. Lett.* 2023, 130(26):263801.
[39] Wang W, Wang X, Ma G. Extended state in a localized continuum. *Phys. Rev. Lett.* 2022, 129(26):264301.
[40] Wen X, Cho C, Zhu X, Park N, Li J. Nonreciprocal field transformation with active acoustic metasurfaces. *Sci. Adv.* 2024, 10(22):eadm9673.
[41] Wen X, Yip HK, Cho C, Li J, Park N. Acoustic amplifying diode using nonreciprocal Willis coupling. *Phys. Rev. Lett.* 2023, 130(17):176101.
[42] Xin H, Song W, Wu S, Lin Z, Zhu S, *et al*. Manipulating the non-Hermitian skin effect in optical ring resonators. *Phys. Rev. B* 2023, 107(16):165401.
[43] Ke S, Wen W, Zhao D, Wang Y. Floquet engineering of the non-Hermitian skin effect in photonic waveguide arrays. *Phys. Rev. A* 2023, 107(5):053508.

[44] Benalcazar WA, Bernevig BA, Hughes TL. Quantized electric multipole insulators. *Science* 2017, 357(6346):61–66.

[45] Benalcazar WA, Bernevig BA, Hughes TL. Electric multipole moments, topological multipole moment pumping, and chiral hinge states in crystalline insulators. *Phys. Rev. B* 2017, 96(24):245115.

[46] Cao W, Wang C, Chen W, Hu S, Wang H, *et al*. Fully integrated parity-time-symmetric electronics. *Nat. Nanotechnol*. 2022, 17(3):262–268.

[47] Liu B, Li Y, Yang B, Shen X, Yang Y, *et al*. Experimental observation of non-Hermitian higher-order skin interface states in topological electric circuits. *Phys. Rev. Res.* 2023, 5(4):043034.

[48] Liu S, Shao R, Ma S, Zhang L, You O, *et al*. Non-Hermitian skin effect in a non-Hermitian electrical circuit. *Research* 2021, 2021:5608038.

[49] Lee CH, Imhof S, Berger C, Bayer F, Brehm J, *et al*. Topolectrical circuits. *Commun. Phys.* 2018, 1(1):39.

[50] Sahin H, Jalil MBA, Lee CH. Topolectrical circuits—recent experimental advances and developments. *APL Electron. Devices* 2025, 1(2):021503.

[51] Sahin H, Akgün H, Siu ZB, Rafi-Ul-Islam SM, Kong JF, *et al*. Protected chaos in a topological lattice. *Adv. Sci.* 2025, 12(28):e03216.

[52] Guan F, Guo X, Zeng K, Zhang S, Nie Z, *et al*. Overcoming losses in superlenses with synthetic waves of complex frequency. *Science* 2023, 381(6659):766–771.

[53] Kim S, Peng Y, Yves S, Alù A. Loss compensation and superresolution in metamaterials with excitations at complex frequencies. *Phys. Rev. X* 2023, 13(4):041024.

[54] Guan F, Guo X, Zhang S, Zeng K, Hu Y, *et al*. Compensating losses in polariton propagation with synthesized complex frequency excitation. *Nat. Mater*. 2024, 23(4):506–511.

[55] Zeng K, Wu C, Guo X, Guan F, Duan Y, *et al*. Synthesized complex-frequency excitation for ultrasensitive molecular sensing. *eLight* 2024, 4(1):1.

[56] Zhu X, Wang H, Gupta SK, Zhang H, Xie B, *et al*. Photonic non-Hermitian skin effect and non-Bloch bulk-boundary correspondence. *Phys. Rev. Res.* 2020, 2(1):013280.

[57] Zhu B, Wang Q, Leykam D, Xue H, Wang Q, *et al*. Anomalous single-mode lasing induced by nonlinearity and the non-Hermitian skin effect. *Phys. Rev. Lett.* 2022, 129(1):013903.